Received 24 August 2023; revised 2 December 2023; accepted 29 December 2023.
Date of publication 4 January 2024; date of current version 26 January 2024.

Digital Object Identifier 10.1109/OAJPE.2024.3349631

Loadability Analysis of Smart Solid-State Transformer Considering Its Interactions Amongst All the Ports

JUNRU CHEN[1] (Member, IEEE), YI ZHANG[1] (Student Member, IEEE), MUYANG LIU[1] (Member, IEEE), YUTIAN CHEN[1] (Student Member, IEEE), AND RONGWU ZHU[2] (Senior Member, IEEE)

[1]School of Electrical Engineering, Xinjiang University, Ürümqi 830046, China
[2]Department of Electrical Engineering, Harbin Institute of Technology Shenzhen, Shenzhen 518055, China
CORRESPONDING AUTHOR: M. LIU (muyang.liu@xju.edu.cn)

ABSTRACT Smart solid-state transformers (STs) have been proposed to modernize the distributed renewable resources dominated distribution system and facilitate the integration of different subsystems/resources as an energy hub/router. A solid power deliver amongst these integrated subsystems is critical to maintain the power balance and to ensure the ST stable operation, while the research on ST loadability analysis is insufficient. Generally, the ST is composed of three-stage offering medium voltage alternative current (MVAC), medium voltage direct current (MVDC), low voltage direct current (LVDC) and low voltage alternative current (LVAC) connectivity. Although the voltage at each port is independently controlled, the power conversion among these ports is electrically coupled and constrained by the maximum deliverable power of each stage. This paper analyzes the operating points of the ST stage by stage with respect to its loadbility and defines the stable operational region of the ST considering the interactions amongst these stages. Moreover, effects of the current limits, voltage regulation and reactive power compensation on the ST loadability and stability enhancement are considered. RT-Lab platform serves to verify the stable operation region of the ST and the efficiency of the above loadability enhancement methods.

INDEX TERMS Equilibrium point, loadability enhancement, power-voltage curve, smart solid-state transformer.

I. INTRODUCTION

A. MOTIVATION

THE Smart solid-sate transformer (ST) has undergone a rapid development in the transition of electricity systems toward higher renewable penetration [1]. Superior to the lower frequency transformer (LFT), the ST has multiple ports with the mixture of alternative current (AC) and direct current (DC) connectivity at both Low voltage (LV) and medium voltage (MV) level [2], which acts like an energy router [3] to integrate not only the transmission and distribution system as LFT did, but also the renewable systems [4], energy storage systems [5], [6] and electric vehicle charging stations [7]. The voltage of these ports can be controlled independently within certain limits.

Besides a integration of different types of systems, another benefit from ST over LFT is the advanced services provision, e.g., power flow control, power factor correction [8], harmonics compensation [9], demand regulation [10], resonance stabilizing, etc.. However, fundamentally, the ST is still a transformer, of which main purpose is to form the voltage fitting into the connected subsystems and to deliver the demanded power amongst subsystems. A stable equilibrium point for the ST operation is critical to maintain a stable power exchange amongst these subsystems, but the study on the ST equilibrium point is insufficient. This paper aims to fill this gap through a systematic loadability analysis of ST.

B. LITERATURE REVIEW

The maximum deliverable power or loadability analysis was referred to the Static Voltage stability in the conventional power system analysis, which can identify the boundary of a stable operation for a system under a certain voltage [11].

It consists in studying whether the power can stably deliver from one bus to another with assigned power flow and studying the how the bus voltages vary as a function of the power delivery, commonly named as power-voltage (P-V) curve. Based on this concept, the loadability of the LFT with tap changer [12] and of the static synchronous compensator (STATCOM) has been widely analyzed in literature [13], [14]. Besides the loadability analysis in the conventional system, considering the distributed energy resources (DERs) generation, the loadability of the microgrid [15] and AC-DC hybrid microgrid [16] has also been analyzed based on the concept of the voltage stability.

However, differs to the LFT, the ST has three stages, including MVAC/MVDC stage: primary side converter (PSC), isolated MVDC/LVDC stage: dual active bridges (DABs) configured by input parallel and output series, and LVDC/LVAC stage: secondary side converter (SSC). Due to the mixed AC and DC loading and renewable generation distributed in each stage, the power routing amongst the three-stage ST is complicated and has divided into three parts accordingly. For this work, the maximum deliverable power of a grid-feeding converter, similarly to the PSC, was analyzed in [17]. Regards to the DC/DC technology, reference [18] analyzes the small-signal voltage stability of a dual-active-bridge (DAB) at a specific equilibrium point using the impedance-based method. Reference [19] analyzes the loadability of a back-to-back converter (i.e. HVdc or a two-stage ST), but neglecting the control constraints in terms of current limits and modulation limits in the converters. Reference [20] proves that the power delivery characteristics of the ST is better than that of the LFT in terms of the AC power delivery. However, the loadability analysis of a complete three-stage ST e in previous literature is insufficient. References [21] and [22] provides a dynamic model of the ST and [23] firstly analyzes the equilibrium point of the ST, but fall to take the electrical coupling amongst three stages and the constraints from the ST inherent controls into the consideration, which may lead to the instability evolving from one stage to others.

C. NOVELTIES AND CONTRIBUTIONS

Based on the concept of the voltage stability, this paper analyzes the loadability of the ST considering not only the ST electric circuit constraints but also its control effects. The specific contributions of this paper are summarized as follows:

- Proposes a general static voltage stability model for the three-stage ST, considering the power delivering and exchanging amongst AC and DC four ports.
- Provides a comprehensive assessment of the voltage stability on the three-stage ST, considering the coupling amongst three stages and its inherent limitations.
- Discusses the voltage stability enhancement methods of the ST in different stages.

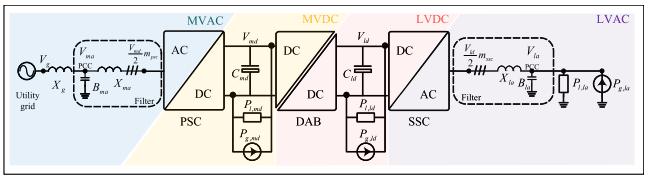

FIGURE 1. **Architecture of the three-stage ST.**

D. ORGANIZATION

The remainder of this paper is organized as follows. Section II reviews the configuration and control of a three-stage ST. Section III proposes a general model for the three-stage ST voltage stability analysis and based on the proposed model the ST voltage stability is analyed stage by stage. Section IV discusses the methods to enhance the ST voltage stability. Section V verifies the theoretical analysis via the simulation in Matlab/Simulink. Finally, Section VI draws the conclusion.

II. REVIEW ON ST CONFIGURATION AND CONTROLS

Figure 1 shows the configuration of the three-stage ST, consisting of PSC, DAB and SSC three stages with MVAC, MVDC, LVDC, LVAC four ports. The basic control of the converters in the three-stage ST is to stabilize the voltage at each port and to manage the power flow amongst subsystems. PSC is a grid-following converter and converts MVAC to MVDC. At the MVAC side, PSC connects to the utility grid V_g via a LC filter B_{ma},X_{ma} and grid impedance X_g and behaves like a PQ bus, achieving the grid synchronization at the voltage of the point of the common coupling (PCC) V_{ma} and actively controlling the grid power exchange P_{ma},Q_{ma} at V_{ma}. At the MVDC side, PSC behaves like a voltage source at the MVDC side actively controlling the MVDC voltage V_{md} dropping on the capacitor C_{md}. DAB converts MVDC to MVDC and behaves like a voltage source at the LVDC side actively controlling the LVDC voltage V_{ld} dropping on the capacitor C_{ld}. SSC is a grid-forming converter and converts LVDC to LVAC, which behaves like a slack bus actively forming the PCC voltage V_{la} after the LC filter B_{la},X_{la}. The MVDC, LVDC and LVAC port voltage are fully controlled while the MVAC voltage is determined by the grid, thus, the distributed energy source and loads can be connected to these ports, e.g. $P_{g,md}$,$P_{l,md}$,$P_{g,ld}$,$P_{l,ld}$,$P_{g,la}$,$Q_{g,la}$,$P_{l,la}$,$Q_{l,la}$ as shown in Fig. 1.

The voltage and output impedance at each port limits the power exchange between the ST and corresponding subsystem. The total power input to and output from ST must be balanced, otherwise the ST becomes unstable. The analysis of the power and voltage relationship and the interaction amongst the subsystem will be detailed in Section III. The upper controls or the extra services of the ST related to the voltage stability at fundamental frequency are briefly reviewed here. The ST only delivers the active power while the reactive power at each port is decoupled. Due to this feature, the ST at primary side can support the MVAC voltage

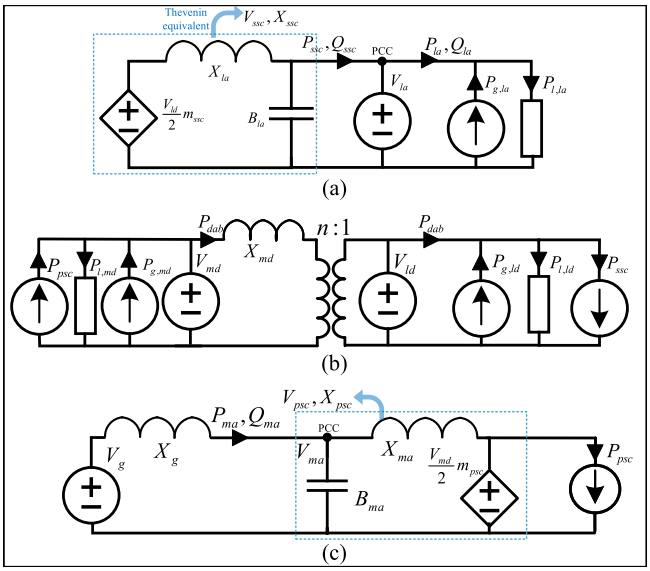

FIGURE 2. ST modeling of (a) SSC, (b) DAB, and (c) PSC.

via reactive power compensation [8]. The DAB uses droop control to slip the DC voltage in order to coordinate with the subsystem for the bidirectional power flow [13]. The SSC can purposely regulate the flexible demand by varying its output voltage amplitude [10] or frequency. Such actions obviously change the power flow in the ST, thus, affecting the voltage stability. The detailed effect of these upper controls on the ST voltage stability will be analyzed in Section IV.

III. ST MODELING AND LOADABILITY ANALYSIS

The voltage stability aims to identify the existence of the stable equilibrium point at fundamental frequency. The P-V curve is normally used to show the relationship between the voltage and power at the discussed bus, where the saddle-node bifurcation (SNB) point represents the maximum deliverable power. Based on this methodology, this section analyzes the loadability of the ST experiencing a large-signal disturbance. Since the loading and generation at the DC parts are pure active power, and also the DAB only deliveries the active power but isolates the reactive power flow, here we focus on the loadability analysis of the active power based on the P-V curve. Of course, the reactive power effects on the AC ports are still taken into the consideration and will be detailed in Section IV. The ST has three stage with classified four ports, correspondingly, the ST is modeled in three parts with controlled sources to represent its internal relationship amongst each port as shown in Fig. 2. Based on these models, this section will analyze the ST voltage in each part separately. Note defining the direction of the power flow from up-stage to down-stage is positive.

A. SECONDARY SIDE CONVERTER

The SSC is the rear-end part of the entire three-stage ST system to only deliver the needed power P_{la}, Q_{la} in the LVAC subsystem. Because of the decoupled power in the SSC to other subsystems, its loadability is analyzed first.

SSC actively controls the LVAC voltage at PCC as a slack bus, feeding the power to the loads $P_{l,la}$, $Q_{l,la}$ at the LVAC side or delivering the DERs generation $P_{g,la}$, $Q_{g,la}$ shown in Fig. 2 (a), where the controlled voltage source $v_{ld}m_{ssc}/2$ before the LC-filter models the SSC terminal voltage determined by its modulation m_{ssc}, of which value is regulated to enforce the SSC output voltage at the PCC tracking to the reference. Thus, the voltage source v_{la} represents the SSC output voltage. The SSC shall output a fixed voltage to the LVAC subsystem as the black horizontal line shown in Fig. 3. The DERs, e.g. wind turbine and PV panel, behave like a constant power source as shown by the cyan line in Fig. 3. The loads have voltage dependent characteristics, and thus they are unified to an exponential model. The power at LVAC with respect to the subsystem is computed as follows:

$$P_{la} = P_{l,la} - P_{g,la} = P_{l,la0}\left(\frac{V_{la}}{V_{la0}}\right)^{\alpha_{la}} - P_{g,la} \tag{1}$$

$$Q_{la} = Q_{l,la0}\left(\frac{V_{la}}{V_{la0}}\right)^{\beta_{la}} - Q_{g,la} \tag{2}$$

where $P_{l,la0}$ and $Q_{l,la0}$ are the loading active and reactive power at the nominal voltage V_{la0}; α_{la} and β_{la} are the voltage coefficients. For example, $\alpha_{la} = \beta_{la} = 2$ represents constant resistance load and $\alpha_{la} = \beta_{la} = 0$ represents constant power load as shown the pink and cyan line in Fig. 3 respectively.

For the LVDC/LVAC stage, the SSC only directly controls the terminal AC voltage, of which value is determined by a modulation signal to the LVDC voltage as shown in Fig. 2. This limits the maximum allowable power conversion of the SSC. As seen in Fig. 2 (a), the Thevenin equivalent circuit of the SSC terminal voltage with the filter as seen by the LVAC voltage at the PCC can be calculated as follows:

$$X_{ssc} = \frac{1}{1 - B_{la}X_{la}}X_{la} \tag{3}$$

$$V_{ssc} = \frac{1}{1 - B_{la}X_{la}}\frac{V_{ld}}{2}m_{ssc} = \frac{X_{ssc}}{X_{la}}\frac{V_{ld}}{2}m_{ssc} \tag{4}$$

where X_{la} and B_{la} are the filter reactance and susceptance, respectively; m_{ssc} is the SCC modulation signal in the phasor frame.

Then the power conversion P_{ssc}, Q_{ssc} from SSC to LVAC network can be computed as:

$$P_{ssc} = \frac{V_{la}V_{ssc}}{X_{ssc}}sin\delta_{ssc} \tag{5}$$

$$Q_{ssc} = -\frac{V_{la}^2}{X_{ssc}} + \frac{V_{la}V_{ssc}}{X_{ssc}}cos\delta_{ssc} \tag{6}$$

where V_{ssc} and δ_{ssc} are the voltage amplitude and angle of the SSC leg output voltage.

By eliminating δ_{ssc} in (5)and (6), the LVAC voltage with respect to the SSC power conversion can be obtained:

$$V_{la} = \sqrt{\frac{V_{ssc}^2}{2} - X_{ssc}Q_{ssc} \pm C_1} \tag{7}$$

where $C_1 = \sqrt{\frac{V_{ssc}^4}{4} - X_{ssc}^2P_{ssc}^2 - X_{ssc}Q_{ssc}V_{ssc}^2}$.

Since the converted power is used to feed the loading in the LVAC distribution system (i.e. in case of neglecting the power losses in the SSC and LC filter, $P_{ssc} = P_{la}$, $Q_{ssc} = Q_{la}$), and the SSC modulation is less than 1, ($m_{ssc} \leq 1$), substituting these quantities into (3) and (4), one obtains the operational region of the LVAC voltage, V_{la}, with respect to the SSC conversion. Note, the P-V curve of the constraints from this SSC conversion (8) and latter from the current limitation and from the modulation in synchronous frame as shown in Fig. 5 are symmetrical, which represents the directional power flow in SSC. However, since in this paper the loading is assumed to be greater than the DER generation at the LVAC side, here we only show the zoom-in results of the positive power part in Fig. 3 to clearly illustrate the movement of the operating point.

$$\sqrt{\frac{V_{ld}^2 X_{ssc}^2}{8X_{ssc}^2} - X_{ssc}Q_{la} - C_2} \leq V_{la} \leq \sqrt{\frac{V_{ld}^2 X_{ssc}^2}{8X_{ssc}^2} - X_{ssc}Q_{la} + C_2} \tag{8}$$

where $C_2 = \sqrt{\frac{V_{ld}^4 X_{ssc}^4}{64X_{la}^4} - X_{ssc}^2 P_{la}^2 - X_{ssc}Q_{la}\frac{V_{ld}^2 X_{ssc}^2}{4X_{la}^2}}$

Note, even the voltage is saturated in the phasor frame, SSC can still be stable but with a high harmonics. However, the SSC cannot deliver more power after the modulation is saturated. Assuming the LVDC voltage is the reference at 0 rad, then the Thevenin equivalent circuit of the SSC in the synchronous frame can be obtained as follows:

$$\frac{X_{ssc}}{X_{la}}\frac{V_{ld}}{2}m_{d,ssc} = V_{la} + X_{ssc}\frac{Q_{la}}{V_{la}} \tag{9}$$

$$\frac{X_{ssc}}{X_{la}}\frac{V_{ld}}{2}m_{q,ssc} = X_{ssc}\frac{P_{la}}{V_{la}} \tag{10}$$

where $m_{d,ssc}$,$m_{q,ssc}$ is the modulation in the synchronous frame. The the boundary of the maximum deliverable power in the SSC can be computed via that the modulation in d-axis and in q-axis is saturated, i.e. $m_{d,ssc} = \pm 1$ or $m_{q,ssc} = \pm 1$, as indicated in (11) and (12), corresponding to the red horizontal line and red slope line in Fig. 3 respectively.

$$V_{la} \leq \frac{V_{ld} + \sqrt{4V_{ld}^2 - 16(1 - B_{la}X_{la})X_{la}Q_{la}}}{4(1 - B_{la}X_{la})} \tag{11}$$

$$V_{la} \leq \frac{2X_{la}P_{la}}{V_{ld}} \tag{12}$$

Note, the modulation limitation in the synchronous frame is tangent to that in the phasor frame as shown in Fig. 3. The LVAC voltage is constrained by the LVDC voltage. The LVDC voltage reduction shrinks the SSC operational region as indicated in (11), thus, the LVDC voltage collapse would make the LVAC voltage instability after. In Fig. 3, the P-V curve shows that the SSC at the LVAC port operates along the solid black horizontal line. As long as the loading characteristic curve crosses the SSC operation line within the red triangle region, the SSC is stable. If the operating points

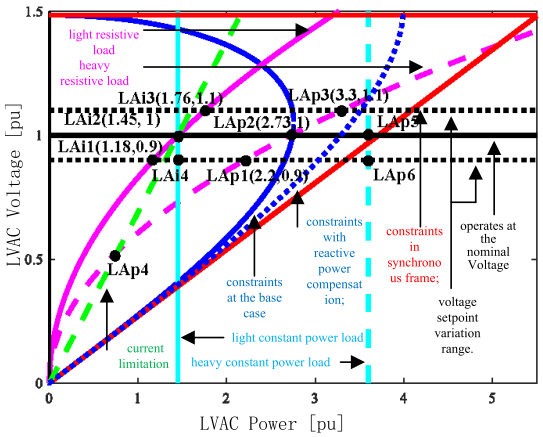

FIGURE 3. SSC operation–the P-V curve of the LVAC.

locates between the blue curve and red triangle line, SSC is still stable but its output contains a significant harmonics, e.g. operating point LAp5.

Remarks: The condition of a stable equilibrium point at the LVAC is that its loading/generation at the reference voltage must be within the operational region of the SSC.

B. DUAL ACTIVE BRIDGE

The DAB is the mid part of the three-stage ST, which actively controls the LVDC voltage V_{ld}, while the MVDC voltage V_{md} is controlled by the PSC, thus they are modelled as the voltage sources shown in Fig. 2 (b). The power bidirectionally flows through the DAB is realized by the phase-shift angle d_{dab} as given in (13).

$$P_{dab} = \frac{V_{md}V_{ld}nd_{dab}(1 - d_{dab})}{2X_{dab}} \tag{13}$$

where n is the transform ratio of the DAB high-frequency transformer and X_{dab} is the DAB impedance at the switching frequency.

The range of d_{dab} ($-0.5 \leq d_{dab} \leq 0.5$) limits the DAB operation boundary, corresponding to the two red lines in Fig. 4. Note, in comparison with downstream power delivery, the DAB is possible to deliver more power to the upstream.

Similar with the LVAC side, at the LVDC side, DERs and DC loads are both connected. Again, defining $P_{g,ld}$, $Q_{g,ld}$ are the power generation by the DERs and $P_{l,ld}$, $Q_{l,ld}$ are the loading at the LVDC side. Besides, DAB delivers the power prosumed in the SSC. Thus, the delivered power in DAB between MVDC to LVDC is:

$$P_{dab} = P_{ssc} + P_{l,ld} - P_{g,ld} \tag{14}$$

Fig. 4 shows the P-V curve of the DAB operation at the LVDC side. The DAB operates along with the black horizontal line. As long as the converted power crosses the DAB operation line in the red del region, the DAB is stable.

Remarks: The condition of a stable equilibrium point at the LVDC is that its loading/generation plus the SSC power demand at the reference voltage must be within the operational region of the DAB.

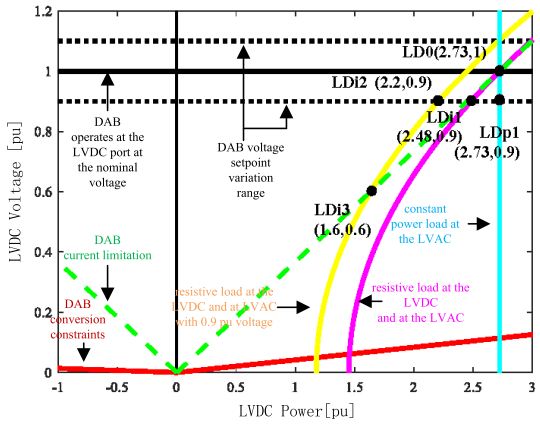

FIGURE 4. DAB operation: the P-V curve at the LVDC.

C. PRIMARY SIDE CONVERTER

The PSC is the front-end part of the three-stage ST system, controlling the power exchange P_{ma},Q_{ma} between the ST and the utility grid at PCC as shown in Fig. 2 (c). Similarly, the active power conversion in PSC consists of the loading $P_{l,md}$ and DER generation $P_{g,md}$ at the MVDC side and the power P_{dab} flowing into the DAB as indicated in (15). While the reactive power conversion in PSC is independently determined by the PSC itself. The PSC terminal voltage $v_{md}m_{psc}/2$ is modulated to achieve above power conversion.

$$P_{psc} = P_{dab} + P_{l,md} - P_{g,md} \tag{15}$$

Differs to other ports, the MVAC voltage is dynamically and indirectly controlled, of which value is the consequence of the grid power exchange. A stable MVAC voltage is important to balance the power in overall subsystems of the ST. Taking the MVAC voltage of the PSC as the observation point, then the equivalent model of the PSC is shown in Fig. 2.

Assuming that, in steady state, the initial phase angle of the PSC voltage at MVAC point V_{ma} is 0 and of the grid voltage V_g is $-\delta_g$. Then the ST power exchanged with the MVAC grid can be computed as follows:

$$P_{ma} = \frac{V_{ma}V_g}{X_g} sin\delta_g \tag{16}$$

$$Q_{ma} = \frac{V_{ma}^2}{X_g} - \frac{V_{ma}V_g}{X_g} cos\delta_g \tag{17}$$

By eliminating δ_g, the P-V curve of the three-stage ST at PCC with respect to the MVAC grid can be obtained as black curve in Fig. 5.

$$V_{ma} = \sqrt{\frac{V_g^2}{2} + X_g Q_{ma} \pm \sqrt{\frac{V_g^4}{4} - X_g^2 P_{ma}^2 + X_g Q_{ma} V_g^2}} \tag{18}$$

It can be seen from (18) that the MVAC voltage is tightly related to the grid state, i.e. grid voltage and grid impedance. The maximum allowable power with respect to the grid state can be obtained as:

$$P_{ma,max} = \frac{1 + sin\varphi}{cos\varphi} \frac{V_g^2}{2X_g} \tag{19}$$

where $\varphi = tan^{-1}\frac{Q_{ma}}{P_{ma}}$.

The power exchange should be within [$-P_{ma,max}$, $P_{ma,max}$] in order to ensure a solid equilibrium point. Otherwise, the instability occurs. Inversely, when the power from the rest part of the ST is informed, i.e. P_{psc}, then the minimum grid voltage of the ST remaining stable is in the situation of $P_{o,max} = P_{psc}$, which is:

$$V_{g,min} = \sqrt{\frac{2P_{psc}^2 X_g}{\sqrt{P_{psc}^2 + Q_{ma}^2} + Q_{ma}}} \tag{20}$$

As long as grid voltage is greater than $V_{g,min}$, the ST is stable on the grid power exchange.

On the other hand, the power exchanged between the MVAC grid and the MVDC of ST is converted via PSC, of which voltage limits the maximum allowable power conversion in PSC. Similar with the computation of the SSC operational region, the Thevenin equivalent circuit of the PSC terminal voltage with the filter as seen by the MVAC voltage at the PCC can be obtained:

$$X_{psc} = \frac{1}{1 - B_{ma}X_{ma}} X_{ma} \tag{21}$$

$$V_{psc} = \frac{1}{1 - B_{ma}X_{ma}} \frac{V_{md}}{2} m_{ma} = \frac{X_{psc}}{X_{ma}} \frac{V_{ma}}{2} m_{ma} \tag{22}$$

Similar to (8)-(12), the operational region of PSC can be computed as (23)-(25) and shown the symmetric blue cardioid and red triangle region in Fig. 5 correspondingly.

$$\sqrt{\frac{V_{md}^2 X_{psc}^2}{8X_{ma}^2} - X_{psc}Q_{ma} - C_3} \le V_{ma} \le \sqrt{\frac{V_{md}^2 X_{psc}^2}{8X_{ma}^2} - X_{psc}Q_{ma} + C_3} \tag{23}$$

$$V_{ma} = \frac{V_{md} + \sqrt{4V_{md}^2 - 16(1 - B_{ma}X_{ma})X_{ma}Q_{ma}}}{4(1 - B_{ma}X_{ma})} \tag{24}$$

$$V_{ma} = \frac{2X_{la}P_{ma}}{V_{md}} \tag{25}$$

where $C_3 = \sqrt{\frac{V_{md}^4 X_{psc}^4}{64X_{ma}^4} - X_{psc}^2 P_{ma}^2 - X_{psc}Q_{ma}\frac{V_{md}^2 X_{psc}^2}{4X_{psc}^2}}$.

Fig. 5 shows the P-V curve of the PSC operation at the MVAC side. The PSC at the MVAC port operates along the black curve. As long as the converted power crosses the PSC operation line in the red triangle region, the PSC is stable. The ST total power or the converted power via PSC at the MVAC port should keep invariant regardless the grid state as represented the solid cyan line in Fig. 5. When the grid voltage is at the nominal, the PSC works along the solid black line and crossed with the loading at the equilibrium point MA0. However, when the grid voltage reduces to $V_{g,min}$ as

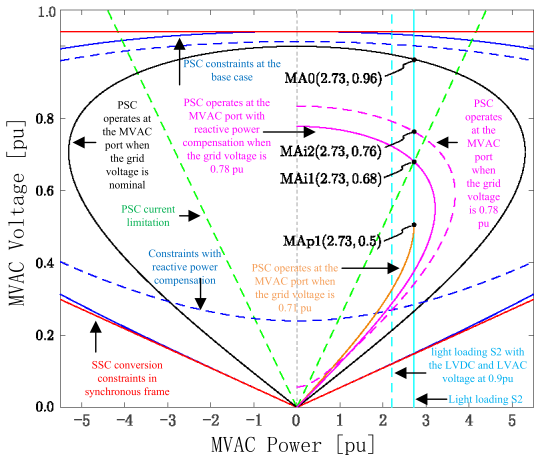

FIGURE 5. PSC operation: the P-V curve at the MVAC.

shown in solid yellow curve, P_{psc} hits the maximum value $P_{ma,max}$ at the equilibrium point MAp1. A further grid voltage reduction will lead to the equilibrium point disappearing, and the loading at the MVDC side of the PSC is greater than the power delivering to the PSC from the grid. The MVDC voltage collapses first in order to compensate the unbalanced power, as a consequence, the LVDC and LVAC voltage collapses and the ST loses stability.

Remarks: The condition of a stable equilibrium point at the MVAC is that the ST total loading/generation can successfully be fed from or feed into the grid meanwhile within the operational region of the PSC.

The loadability and stability analysis in this section is based on the ideal conditions, emphasizing electric links amongst stages and subsystems as modelled in Fig. 2, without considering the impacts and constraints from a real control system of ST, of which will be discussed in following section.

IV. EFFECT OF THE ST CONTROLS ON ITS LOADABILITY

Since the loadability of the ST mainly depends on the power conversion in each stage and the voltage level at each port, some of ST controls would vary the ST terminal voltage and then change the power flow, thus affecting the loadability of entire ST. This section will analyze the effect of these controls on the ST loadability, including the current limitation, voltage setpoint variation and reactive power compensation.

A. CURRENT LIMITATION

Converters have restriction on the current setpoint to avoid overcurrent damage. The current limitation is normally implemented inside the current control loop of the PSC and SSC, and limited by the phase shift angle in the DAB. When the overcurrent occurs due to the fault or overloading, they switch to work in a current-control mode with a current saturation, $I_{md,x}^2 + I_{mq,x}^2 = I_{m,x}^2$. This introduces an additional constraint in the PSC, DAB and SSC as the dashed green line shown in Fig. 3 - Fig. 5.

$$-I_{md,x}V_x \leq P_x \ll I_{md,x}V_x \tag{26}$$

where subscript "x" represents to the "PSC", "DAB" and "SSC", respectively.

For the SSC, it can be seen in Fig. 3 that the operating point LAp2 locates outside of the satisfied current region, thus, becomes unreachable. Due to the overloading, the SSC turns to operate along with the dashed green line and crossing with the dashed pink loading curve at new equilibrium point LAp4. This action although reduces the loading, which benefits to the stability, the LVAC voltage is reduced significantly. According to the grid code requirement, the LVAC voltage shall be within 1.0 ± 0.1pu, of which satisfied region is bounded by two dashed black horizontal line in Fig. 3. Obviously, equilibrium point LAp4 is not satisfied; consequently, the under-voltage relay traps and load curtailment occurs.

For the DAB, differs to the nature limitation of the phase shift angle ($-0.5 \leq d_{dab} \leq 0.5$), the current limitation enforces a symmetric boundary for both the generation and loading. The effect of the current limitation on DAB is the same as that on SSC.

For the PSC, when the grid voltage reduces, the current limitation reduces the capability of the PSC power conversion. After the MAi1 in Fig. 5, the loading of the ST cannot be hold and PSC turns to operate along with the dashed green line. If the loading of entire ST does not reduce thereby, the power balance in ST is broken, resulting in the instability. For example, operating point MAp1 now is unstable. The MVAC voltage of the operating point MAi1 is:

$$V_{ma} = P_{psc}/I_{md,psc} \tag{27}$$

Substituting (27) into (18) can obtain the critical grid voltage for a stable PSC operation:

$$\begin{aligned} V_{g,min} &= \sqrt{\frac{X_g^2\left(P_{psc}^2 + Q_{psc}^2\right)}{V_{ma}^2} + V_{ma}^2 - 2Q_{psc}X_g} \\ &= \sqrt{X_g^2 I_{m,psc}^2 + V_{ma}^2 - 2Q_{psc}X_g} \end{aligned} \tag{28}$$

Remarks: The inclusion of the current limitation in ST narrows its stable operational region and worsens the loadability.

B. VOLTAGE SETPOINT VARIATION

The voltage can be actively set in a range of 1.0 ± 0.1pu in the MVDC, LVDC and LVAC port. This modifies the operation of the SSC and DAB as the dashed black line shown in Fig. 3 - Fig. 4. An active variation of the voltage setpoint can vary the voltage-sensitivity demand and thus help improve the loadability and stability.

For the SSC, in the situation of no current limitation, the voltage variation aims to better coordinate with the LVDC voltage, i.e. the solid blue cardioid in Fig. 3. The voltage reduction for the impedance load lowers the loading, e.g. the equilibrium point changes from LAp3 to LAp2, thus improving the stability of the SSC. However, if the load

is constant power or prosuming, the voltage variance may lead to instability, e.g. the equilibrium point change from LAp5 to LAp6. On the other hand, in the situation of current limitation included, the voltage variation help withdraw the current saturation. For example, the voltage reduction moves the equilibrium point from LAi2 to LAi1.

For the DAB, since the power to SSC is independent to the LVDC voltage, this complicates the voltage variance at the LVDC port for the purpose of the loadability enhancement. For example, even for a DC resistive load as the pink line shown in Fig. 4, the voltage reduction moves the equilibrium point LD0 to an unstable operating point LDi1.

A proper voltage variance reduces the loading power, which benefits the stability not only at the corresponding stage but also at the up-stage. For example, the LVAC voltage reduction from 1.0 to 0.9 pu makes the operating point moving from LAi2 to LAi1 as shown in Fig. 3 and accordingly the loading curve at the LVDC voltage in Fig. 4 moves from the pink line to the yellow line. As consequence, the unstable operating point LDi1 in Fig. 4 relocates to a stable equilibrium point LDi2 when LVDC voltage is at 0.9 pu. This action benefits to the PSC as well by moving the loading curve in Fig. 5 from the solid red line to the dashed red line with a possible lower grid fault voltage.

C. REACTIVE POWER COMPENSATION

Reactive power compensation is a general method to enhance the loadability for the LFT, using FACTS devices. Differently, ST can inherently achieve the reactive power compensation.

For the SSC, it actively forms the LVAC voltage. A simple way to boost the reactive power is to parallel a capacitor or SVC at the PCC. Substituting this additional capacitance ΔB_{la} into (3) and (4) obtains:

$$X_{ssc} = \frac{1}{1-(B_{la}+\Delta B_{la})X_{la}} X_{la} \tag{29}$$

$$V_{ssc} = \frac{1}{1-(B_{la}+\Delta B_{la})X_{la}} \frac{V_{ld}}{2} m_{ssc} \tag{30}$$

where this additional capacitance reduces the equivalent impedance X_{ssc} of the SSC and increases the equivalent voltage V_{ssc}, resulting in a larger operational region from the solid blue cardioid to dashed blue cardioid in Fig. 3.

For the PSC, the reactive power compensation can be directly realized by a V/Q droop. On the one hand, at the grid side, substituting this reactive power compensation ΔQ_{psc} into (20) obtains:

$$V_{g,min} = \sqrt{\frac{2P_{psc}^2 X_g}{\sqrt{P_{psc}^2+(Q_{ma}+\Delta Q_{ma})^2}+Q_{ma}+\Delta Q_{ma}}} \tag{31}$$

where this reactive power compensation can help reduce the minimum grid voltage of the ST remaining stable, i.e. extending the stability boundary. Substituting ΔQ_{psc} into (18) could draw the P-V curve of the SSC at the MVAC voltage with respect to the grid voltage, which increases the loadability

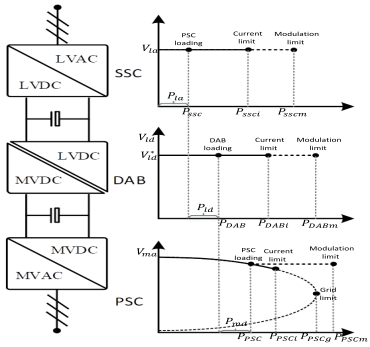

FIGURE 6. ST loadability assessment.

and thus moves the solid pink curve to the dashed pink curve in Fig. 5. On the other hand, at the PSC terminal side, substituting this reactive power compensation ΔQ_{psc} into (24) obtains:

$$V_{ma} = \frac{\sqrt{4V_{md}^2 - 16(1-B_{ma}X_{ma})X_{ma}(\Delta Q_{ma}+Q_{ma})}}{4(1-B_{ma}X_{ma})} + \frac{V_{md}^2}{4(1-B_{ma}X_{ma})} \tag{32}$$

where this reactive power compensation flowing through the PSC filter lowers the upper boundary of the PCC voltage. Substituting ΔQ_{psc} into (23) could draw the P-V curve of the SSC at the MVAC voltage with respect to the PSC terminal voltage, which reduces the operational region and moves the solid blue cardioid to dashed blue cardioid in Fig. 5.

This action could increase the loadability with respect to the grid as indicated in (20), moving the solid pink curve to the dashed pink curve in Fig. 5; but reduce the operational region of the PSC as indicated in (23), moving the solid blue cardioid to dashed blue cardioid in Fig. 5.

V. ST LOADABILITY CRITERIA

Although the loadability analysis is separated into three parts corresponding to ST three stages, there are strong interactions amongst these stages and an improper operation at one stage could lead to the equilibrium point disappearing at other stages. One of the purpose of the loadability analysis is to identify the maximum power delivery at a given grid state. As long as the loading is greater than the maximum deliverable power, the system loses stability. Based on this characteristics, the criteria of the ST loadability is determined in this section.

The ST in the LVAC, LVDC and MVDC behaves like a voltage source and in the MVAC behaves like a constant power load, of which the operating point in SSC and DAB moves along with a horizontal line as indicated before in Fig. 3 and Fig. 4, and in PSC moves along with a curve as indicated before in Fig. 5. Taking the right part of P-V curve as an example, Fig. 6 redraws the stable range of the operating point movement at each stage. The power relationship amongst ST stages is also shown in Fig. 6.

A. MODULATION LIMITATION

From the analysis in Section III, the constraints on the ST loadability from the electrical aspect are the modulation as donated P_{SSCm},P_{DABm},P_{PSCm} in Fig. 6 respectively.

For the SSC, in a stable operation, the LVAC voltage is at its reference value V_{la}^*. The SSC loses stability in the situation of that the delivered power is less than the loading, of which operating point locates outside of the red triangle zone in Fig. 3. Substituting $V_{la} = V_{la}^*$ into (12) could obtain the maximum deliverable power P_{SSCm} in relation to a saturated modulation at the reference LVAC output:

$$P_{SSCm} = V_{ld} V_{la}^* / (2X_{la}) \tag{33}$$

For the DAB, in a stable operation, the LVDC voltage is at its reference value V_{ld}^*. The DAB loses stability in the situation of that the delivered power is less than the loading at the LVDC plus the loading from the PSC, of which operating point locates outside of the red triangle zone in Fig. 4. Substituting $V_{ld} = V_{ld}^*$ into (13) could obtain the maximum deliverable power P_{DABm} in relation to a saturated modulation at the reference LVDC output:

$$P_{DABm} = V_{md} V_{ld}^* n / (8X_{dab}) \tag{34}$$

For the PSC, the MVAC voltage is a consequence of the power exchange between the ST and grid as given in (18). The PSC loses stability in the situation of that the delivered power is less than the loading at the MVDC plus the loading from the DAB, of which operating point locates outside of the red triangle zone in Fig. 5. Substituting $V_{md} = V_{ma}^*$ into (25) could obtain the power P_{PSCm} in relation to a saturated modulation:

$$P_{PSCm} = V_{ma} V_{md}^* / (2X_{ma}) \tag{35}$$

P_{SSCm},P_{DABm},P_{PSCm} are related to the voltage at both sides of the converter. The increase in the voltage setpoint can raise the power tolerance, thus, enhancing the loadability.

If the loading at the port is greater than the power tolerance of the corresponding converter P_{xm}, the converter will become unstable. On the other hand, the converter modulation also limits the downstream voltage with respect to its upstream voltage as indicated before in (11). This is the reason that when the upstream voltage collapses, the downstream voltage collapses following.

B. CURRENT LIMITATION

From the analysis in Section IV, the constraint on the ST loadability from the control aspect is the current limitation as donated P_{SSCi},P_{DABi},P_{PSCi} in Fig. 6, of which value can be calculated in (26).

P_{SSCi},P_{DABi},P_{PSCi} is solely related to the value of the current limits and irrelevant to the voltage at other ports. Note, when the port voltage holds on the setpoint, $P_{xi} < P_{xm}$; however, when the port voltage collapse, $P_{xi} > P_{xm}$.

When the loading at the port is greater than the current limitation of the corresponding converter P_{xi}, the converter loses controllability. If the P-V line of the current limitation crosses to the loading characteristics, the converter is still stable and stays at the crossover point; otherwise, the converter becomes unstable.

C. GRID LIMITATION

ST connects to the grid via PSC, of which interaction was indicated in (16)-(18) before. The power exchange between the ST and grid depends on the grid impedance and grid voltage, of which maximum grid power exchange was computed in (19).

The grid fault would affect to the stability of the ST. The grid voltage sage or the grid impedance increase reduces the maximum allowable power $P_{ma,max}$. When the loading is greater than the maximum deliverable power from the grid, the capacitor at the MVDC will release the power and the MVDC voltage sags, and then the LVDC and LVAC voltage collapse stage by stage due to the saturated modulation. The whole ST and its connected subsystems lose stability after.

From above analysis, a stable operation of the ST is that its port voltages keep on the reference value, i.e. V_{la}^*, V_{ld}^*, V_{md}^* and the loading for each stage is less than its maximum allowable power deliver, i.e. $P_x < min(P_{xi}, P_{xm}, P_{xg})$. On the contrary, if the loading is greater than the maximum allowable power of the corresponding converter, this converter loses controllability and may become unstable, while other stages may still be controllable and stable if its loading within the operational range. However, if the voltage at one port collapse, the downstream port voltages collapse following and the downstream stages loses stability while the upstream port voltage and stages may still be stable if its loading within the operational range.

VI. VALIDATION

A simulation study in RT-Lab platform is used to validate the proposed loadability analysis of the three-stage ST. The tested system is set-up as shown in Fig. 1, where the system parameters and VSC control parameters are given in Table 1 and Table 2 respectively. The validation follows the order of the analysis in Section II and accords with the Fig. 3 - Fig. 5. The base power of the DAB is 10kW, the base voltage is 220V at LVAC side, 800V at LVDC side, 17kV at MVDC side and 10kV at MVAC side. The current limit of the SSC is set to be 32.2A (1pu), that of DAB is 34A or 2.28∘ and of PSC is 3.266A. Note, in order to purposely enforce the ST instability, the grid impedance is set to be significant as well as the PSC filter.

A. SECONDARY SIDE CONVERTER

This section validates the loadability analysis of the ST SSC based on Fig. 3. The system experiences the reference SSC voltage step changes from 0.9pu to 1.0pu at 1s and increases again to 1.1pu at 2s. Three cases are tested:

- ''SSC'' has no current limitation and the LVAC loading is heavy, 5.34Ω, operating along with the dashed pink line in Fig. 3;

TABLE 1. Electrical parameters of three-stage ST.

Parameters	Symbols	Values
MVAC voltage (kV)	V_{ma}	10
MVDC voltage (kV)	V_{md}	17
LVAC voltage (kV)	V_{ma}	0.22
LVDC voltage (kV)	V_{md}	0.8
LVDC voltage (kV)	V_{md}	0.8
MVAC line inductance (mH)	L_g	0.3e3
LVAC line inductance (mH)	L_{ma}	1.8e3
Turn ratio of DC/DC transformer	N	20
Magnetizing inductance of DC/DC transformer (mH)	L_m	19
Switching frequency of DAB (kHz)	f_m	10
MVDC-link capacitance (μF)	C_{md}	13.6
LVDC-link capacitance (μF)	C_{ld}	20
LVAC side filter inductance (mH)	L_{la}	16
LVAC side filter capacitance (μF)	C_{la}	85

TABLE 2. Control parameters of three-stage ST.

Parameters	Symbols	Values
Proportional gain of PSC PLL controller	$k_{p,pll}$	0.022
Integral gain of PSC PLL controller	$k_{i,pll}$	0.39
Proportional gain of PSC current controller	$k_{p,psc}$	3.6e3
Integral gain of PSC current controller	$k_{i,psc}$	2.0e3
Proportional gain of DAB controller	$k_{p,dab}$	1.0e-3
Integral gain of DAB controller	$k_{i,dab}$	2.0e-4
Proportional gain of SSC voltage controller	$k_{p,v-ssc}$	0.09
Integral gain of SSC voltage controller	$k_{i,v-ssc}$	19.3
Proportional gain of SSC current controller	$k_{p,i-ssc}$	3.6e3
Integral gain of SSC current controller	$k_{i,i-ssc}$	2.0e3
SSC switching frequency (kHz)	f_{ssc}	6.3
DAB switching frequency (kHz)	f_{ssc}	10
PSC switching frequency (kHz)	f_{ssc}	18.9
Time step (s)	T_s	5E-8

- "SSC+Q" uses the same loading but adds reactive power compensation by increasing capacitance of the LC filter from $85\mu F$ to $225\mu F$;
- "SSC+I_m" includes current limitation and the LVAC loading is light, 10Ω and the LVDC loading is 50.36 Ω, operating along with the solid pink line in Fig. 3 and Fig. 4.

Fig. 7 shows the results of the active power, current and voltage amplitude at the LVAC port. It can be seen that without current saturation, the heavy loading initially stays at the point LAp1 and moves to LAp2 after the reference voltage increasing to 1pu. However, when the reference voltage increases again, since LAp3 is out of the region of (8), the modulation of the SSC becomes saturated and its terminal voltage presents a head-cut as shown in Fig. 8 (a). In this case, the SSC actually outputs reactive current in order to approach point LAp3 with high harmonics as shown in Fig. 7. A reactive power compensation can enlarge the saturated modulation region to be dashed blue cardioid in Fig. 3 and

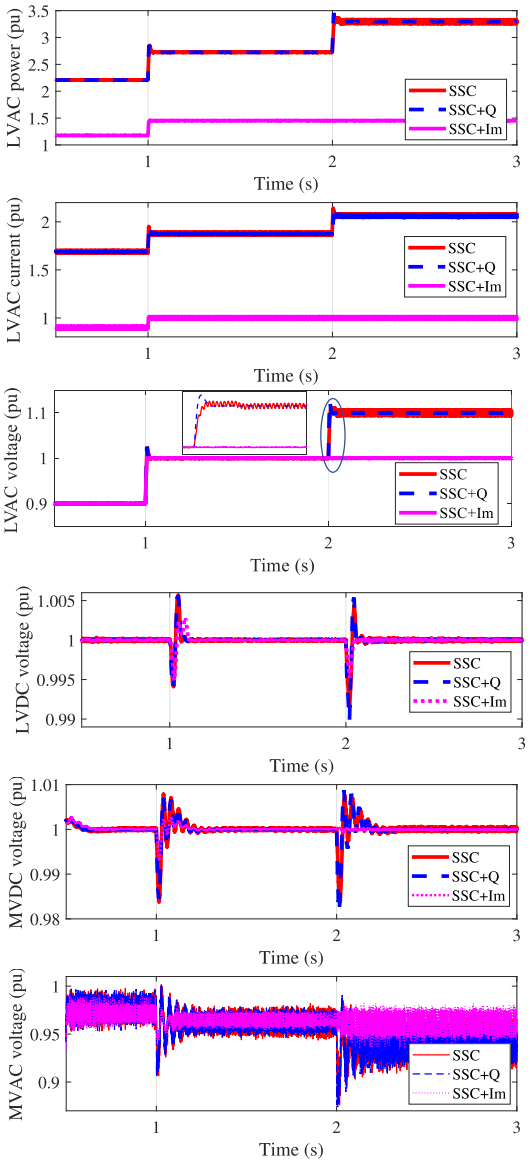

FIGURE 7. SSC, DAB and PSC response during the SCC reference voltage changes.

make LAp3 become a healthy equilibrium point as proved by the blue line in Fig. 7 and in Fig. 8 (b).

The current saturation shrinks the operation range. The light loading initially stays at the point LAi1 with unsaturated current and moves to LAi2 with exact saturated current after the reference voltage increasing to 1pu. A further increase in the reference voltage pushes the operating point to LAi3, which is out of the current saturation so that is unreachable. Since the operating point has to move along with the pink line meanwhile being in the current saturation region, after a transient, it converges back to operating point LAi2 as the pink line shown in Fig. 7.

Fig. 7 shows the results of the voltage amplitude at the LVDC, MVDC and MVDC during this process. The voltages at the up-stages are stable for all the cases. Although the case "SSC" presents high harmonics at the LVAC side, its voltage

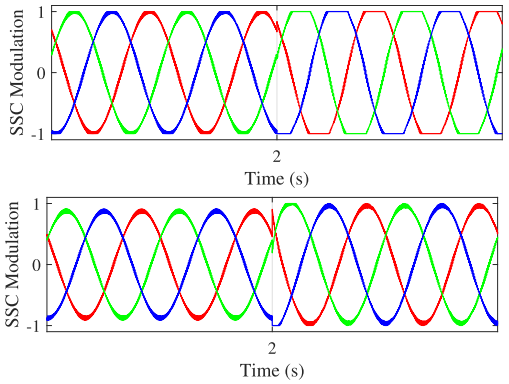

FIGURE 8. LVAC voltage at operating point LAp3, upper Case "SSC" and lower Case "SSC+Q".

at the up-stages is stable and presents the same response as the case "SSC+Q". This is because the loading is identical for the DAB and PSC at these two cases and this loading is within the stable operational region at the equilibrium point LD0 in Fig. 4 and MA0 in Fig. 5 during 1-2s. The MVAC voltage reduces with the loading increase as indicated by the black curve in Fig. 5.

In above cases, the SSC has an operating point during the disturbances and even loses controllability for the case "SSC+I_m", thus, is stable. In order to observe the situation of the instability attributing to the SSC, we add another two cases as follows:

- "SSC" has no current limitation and the LVAC loading is heavy, constant 34 kW, operating along with the dashed cyan line in Fig. 3;
- "SSC+Q" includes current limitation and the LVAC loading is light, constant 14.5 kW, operating along with the solid cyan line in Fig. 3;

Note, there are no current limitation included in the DAB and PSC. The system experiences the LVAC voltage drops from 1 pu to 0.9 pu at 1 s.

Fig. 9 show the response of the SSC and other two stages respectively. It can be seen in Fig. 3 that initially the operating points LAp5 and LAi2 are stable for both cases, after the voltage drops to 0.9 pu, they move to LAp6 and LAi4, which are out of the operational region of the modulation saturation and current limitation respectively. Hence, both cases show instability after 1 s in Fig. 9. Due to unlimited current in DAB, the unstable SSC although outputs oscillating power at the LVAC, this power is still in the operational range of the DAB and PSC, thus, the voltages at the LVDC, MVDC and MVAC are stable at their setpoint but present interacted oscillations as shown in Fig. 9.

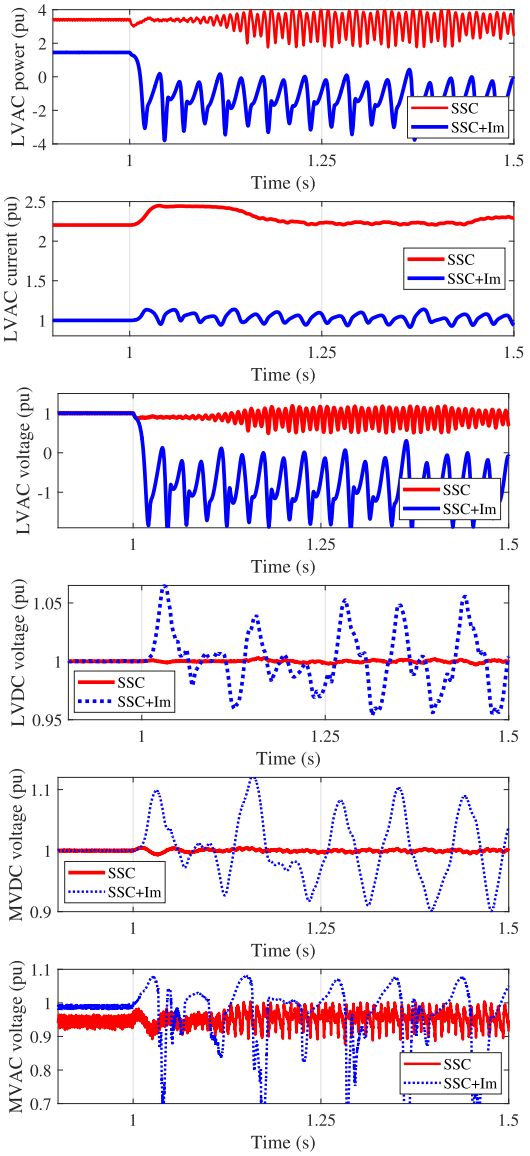

FIGURE 9. SSC, DAB and PSC response during the SSC reference voltage changes.

B. DAB

This section validates the loadability analysis of the DAB in ST based on Fig. 4. The system experiences the reference LVDC voltage step changes from 1.0pu to 0.9pu at 1s. Four cases are tested:

- "DAB" has no current limitation and the loading is 5.34Ω at the LVAC, operating with the cyan line in Fig. 4 and dashed pink line in Fig. 3;
- "DAB+I_m" includes current limitation and the loading is constant 14.5 kW at the LVAC, operating with the cyan line in Fig. 4 and solid cyan line in Fig. 3;
- "DAB+I_m+R_{dc}" includes current limitation and the loading is 10Ω at the LVAC and 50.36 Ω at the LVDC, operating along with the solid pink line in Fig. 3 and Fig. 4;
- "DAB+I_m+R_{dc}+0.9V_{la}" has the same condition with the case "DAB+I_m+R_{dc}" but the LVAC voltage setpoint drops from 1.0pu to 0.9pu, operating along with yellow line in Fig. 4.

Fig. 10 shows the results of active power and voltage at the LVDC port and the voltage at the LVAC port. Initially, the

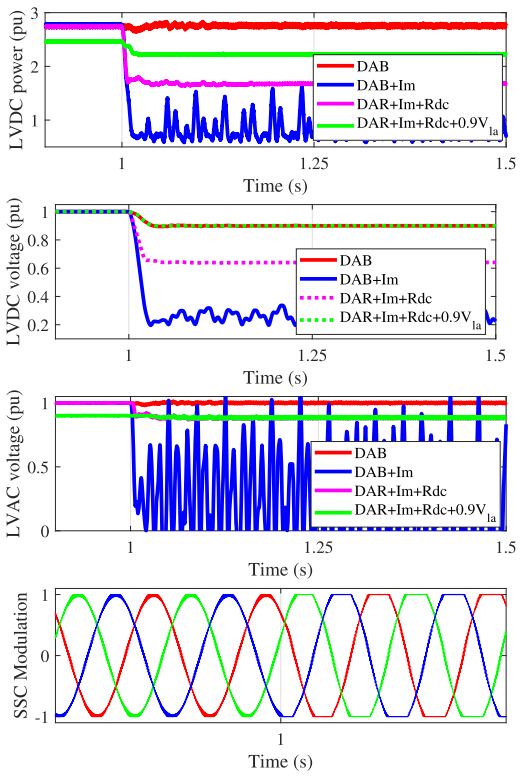

FIGURE 10. DAB response during its reference voltage changes and LVAC voltage at operating point LDp1 (modulation saturated).

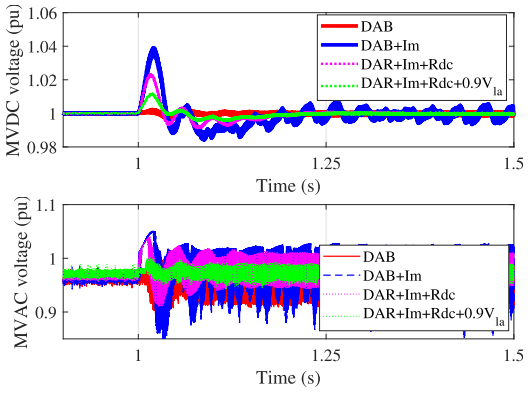

FIGURE 11. PSC response during the DAB reference voltage changes.

TABLE 3. Critical grid voltage and the time of instability occurrence.

Cases	$V_{g,min}$(pu)	Time (s)
PSC	0.71	2.45
PSC+I_m	0.78	2.10
PSC+I_m+Q	0.72	2.40
PSC+I_m+0.9V_{ld}+0.9V_{la}	0.67	2.65

operating point of all cases stays at LD0. For the case "DAB" the LVDC reference voltage reduction moves its operating point to LDp1. However, this loading at the LVAC side stays at a critical operating point LAp2 in Fig. 3, the LVDC voltage reduction narrows the operating region at the LVDC side and makes LAp2 out of a healthy operating region. Similar to the case "SSC" in last section, the SSC terminal voltage becomes saturated as shown in Fig. 10. The inclusion of current saturation at the DAB makes the operating point LAp1 unreachable. As a consequence, the system collapses after the reference voltage reduction and the LVDC voltage sags. This enforces the LVAC voltage to collapse as shown the case "DAB+Im" in Fig. 10.

On the other hand, for the case "DAB+I_m + R_{dc}", the LVDC voltage reduction makes the operating point moving towards LDi1. Since this point locates outside of the current saturation region, the instability occurs and the operating point moves along with the pink line with the LVDC voltage reduction. The lower LVDC voltage saturates the SSC and the LVAC voltage reduces thereby. This movements reduce the loading power at both LVAC and LVDC and result in the pink curve in Fig. 4 moving towards left until crossing with the current limitation and stabilizing at LDi3. Based on this scenario, a voltage reduction at the LVAC side could move the loading curve at the LVDC side from the pink line to the yellow line and the new equilibrium point LDi2 is stable in Fig. 4. Hence a proper action on the SSC can avoid instabilities, i.e. the case "DAB+I_m + R_{dc}" as shown in Fig. 10. Note, since the modulations of the cases "DAB", "DAB+I_m" and "DAB+I_m + R_{dc}" in the phasor frame are saturated, they present a higher harmonics after the reference LVDC voltage changes in Fig. 10.

Fig. 11 shows the results of the voltage amplitude at the MVDC and MVAC during this process. As expected, as long as the loading power is within the operational region of the PSC, the MVDC and MVAC voltages are both stable.

C. PRIMARY SIDE CONVERTER

This section validates the loadability analysis of the PSC in ST based on Fig. 5. In order to show the instability of the PSC at different operations, the system experiences the grid voltage decreases at 1s with 0.2pu/s slope. Four cases are tested with the same loading condition, 10Ω at the LVAC and 50.36Ω at the LVDC:

- "PSC" without current limitation;
- "PSC+I_m" with current limitation;
- "PSC+I_m+Q" with current limitation and a 0.5 pu reactive power compensation;
- "PSC+I_m+0.9V_{ld}+0.9V_{la}" with current limitation and both LVDC and LVAC voltage drop from 1.0pu to 0.9pu.

According to the stability criteria in (20) and (28), the critical grid voltage for an instant instability is computed and recorded in Table 3. Since the slope of the grid voltage reduction is 0.2pu/s starting at 1.0s, the time of the instability occurrence can be correspondingly computed.

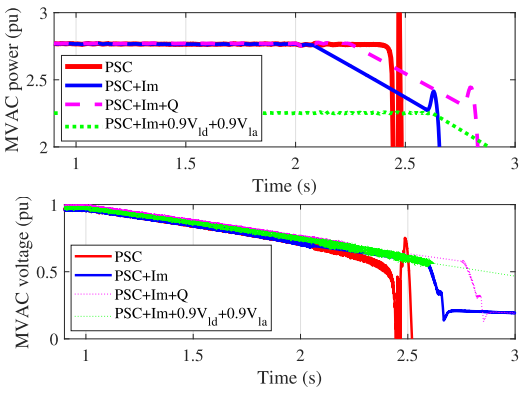

FIGURE 12. **PSC response during the the grid voltage sags.**

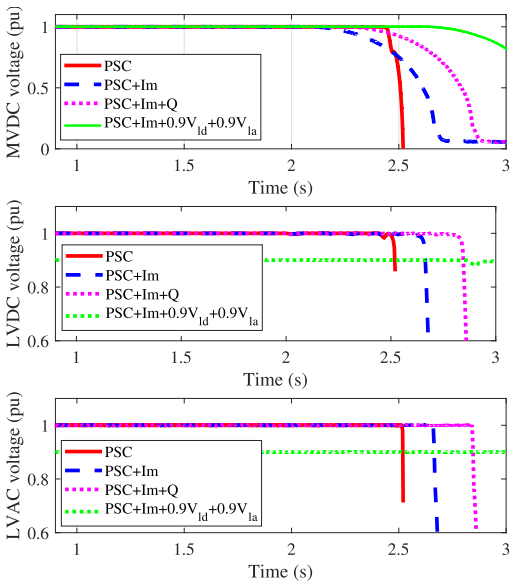

FIGURE 13. **DAB and SSC response during the the grid voltage sags.**

Fig. 12 shows the results of voltage and active power at the MVAC port. Initially, the operating point stays at MA0 with the grid voltage at nominal. Without the current limitation in PSC, the PSC becomes unstable only if the ST total loading is greater than the maximum allowable grid power injection during the fault as the red line shown in Fig. 12 and the point MAp1 in Fig. 5. This critical point could be computed in (16). A current limitation narrows the operational region and its operating curve, green line, crosses to the loading at point MAi1 as computed in (22). After MAi1, the operating point locates outside of the operational region and the ST becomes unstable as shown the blue line in Fig. 12. A reactive power compensation could enhance the loadability by raising the operating point from MAi1 to MAi2 when the grid voltage is 0.78pu. Therefore, the case "PSC+I_m+Q" in Fig. 12 becomes unstable when the grid voltage is 0.72 pu, which is lower than the critical voltage of the case "PSC+Im". However, the reactive power compensation narrows the operational region of the PSC with respect to the MVDC voltage, as reflected in Fig. 5 from the solid to dashed blue cardioid. Besides the reactive power compensation, the voltage regulation in ST can help enhance the loadability as proved in the case "PSC+I_m+0.9V_{ld}+0.9V_{la}". After the MVAC voltage instability occurrence, the rest stages of the ST all become unstable as shown the in Fig. 13.

VII. CONCLUSION

This paper proposes a general model for the three-stage ST loadability analysis and based on this proposed model, the loadability of the three-stage ST with various controls is analyzed. From the validations, this paper draw the following conclusions:

i) As long as the operation of the up-stage of the ST locating in the stable region, the ST is stable even if the down-stage is unstable. However, inversely, if the up-stage is unstable, the down-stage is also unstable.

ii) The current limitation worsens the loadability of the ST by narrowing the operational region.

iii) A proper voltage regulation enhances the loadability on not only the active stage but also the up-stages.

iv) The reactive power compensation can enlarge the operational region and enhance the loadability of the ST. In this paper, we only focus on the effect of the ST operation (current limitation, voltage setpoint variation and reactive power compensation) on its loadability, but does not consider the specific control implementations, i.e. DC automatic voltage regulation in SSC, droop control in DAB and V-Q droop in PSC, which will be further analyzed in the future.

REFERENCES

[1] L. F. Costa, G. De Carne, G. Buticchi, and M. Liserre, "The smart transformer: A solid-state transformer tailored to provide ancillary services to the distribution grid," *IEEE Power Electron. Mag.*, vol. 4, no. 2, pp. 56–67, Jun. 2017, doi: 10.1109/MPEL.2017.2692381.

[2] X. She, A. Q. Huang, and R. Burgos, "Review of solid-state transformer technologies and their application in power distribution systems," *IEEE J. Emerg. Sel. Topics Power Electron.*, vol. 1, no. 3, pp. 186–198, Sep. 2013, doi: 10.1109/JESTPE.2013.2277917.

[3] A. Q. Huang, M. L. Crow, G. T. Heydt, J. P. Zheng, and S. J. Dale, "The future renewable electric energy delivery and management (FREEDM) system: The energy internet," *Proc. IEEE*, vol. 99, no. 1, pp. 133–148, Jan. 2011, doi: 10.1109/JPROC.2010.2081330.

[4] R. Zhu, G. De Carne, F. Deng, and M. Liserre, "Integration of large photovoltaic and wind system by means of smart transformer," *IEEE Trans. Ind. Electron.*, vol. 64, no. 11, pp. 8928–8938, Nov. 2017, doi: 10.1109/TIE.2017.2701758.

[5] X. Gao, F. Sossan, K. Christakou, M. Paolone, and M. Liserre, "Concurrent voltage control and dispatch of active distribution networks by means of smart transformer and storage," *IEEE Trans. Ind. Electron.*, vol. 65, no. 8, pp. 6657–6666, Aug. 2018, doi: 10.1109/TIE.2017.2772181.

[6] C. Kumar, R. Zhu, G. Buticchi, and M. Liserre, "Sizing and SOC management of a smart-transformer-based energy storage system," *IEEE Trans. Ind. Electron.*, vol. 65, no. 8, pp. 6709–6718, Aug. 2018, doi: 10.1109/TIE.2017.2784389.

[7] H. Hua, Y. Qin, C. Hao, and J. Cao, "Stochastic optimal control for energy internet: A bottom-up energy management approach," *IEEE Trans. Ind. Informat.*, vol. 15, no. 3, pp. 1788–1797, Mar. 2019, doi: 10.1109/TII.2018.2867373.

[8] D. Shah and M. L. Crow, "Online volt-var control for distribution systems with solid-state transformers," *IEEE Trans. Power Del.*, vol. 31, no. 1, pp. 343–350, Feb. 2016, doi: 10.1109/TPWRD.2015.2457442.

[9] N. B. Y. Gorla, S. Kolluri, M. Chai, and S. K. Panda, "A comprehensive harmonic analysis and control strategy for improved input power quality in a cascaded modular solid state transformer," *IEEE Trans. Power Electron.*, vol. 34, no. 7, pp. 6219–6232, Jul. 2019, doi: 10.1109/TPEL.2018.2873201.
[10] J. Chen et al., "Impact of smart transformer voltage and frequency support in a high renewable penetration system," *Electric Power Syst. Res.*, vol. 190, Jan. 2021, Art. no. 106836, doi: 10.1016/j.epsr.2020.106836.
[11] T. Van Cutsem and C. Vournas *Voltage Stability of Electric Power Systems*. New York, NY, USA: Springer, 2008.
[12] C. Vournas and M. Karystianos, "Load tap changers in emergency and preventive voltage stability control," *IEEE Trans. Power Syst.*, vol. 19, no. 1, pp. 492–498, Feb. 2004.
[13] E. Ghahremani and I. Kamwa, "Optimal placement of multiple-type FACTS devices to maximize power system loadability using a generic graphical user interface," *IEEE Trans. Power Syst.*, vol. 28, no. 2, pp. 764–778, May 2013.
[14] B. Ismail, N. I. A. Wahab, M. L. Othman, M. A. M. Radzi, K. N. Vijyakumar, and M. N. M. Naain, "A comprehensive review on optimal location and sizing of reactive power compensation using hybrid-based approaches for power loss reduction, voltage stability improvement, voltage profile enhancement and loadability enhancement," *IEEE Access*, vol. 8, pp. 222733–222765, 2020.
[15] X. Xu et al., "Maximum loadability of islanded microgrids with renewable energy generation," *IEEE Trans. Smart Grid*, vol. 10, no. 5, pp. 4696–4705, Sep. 2019.
[16] A. A. Eajal, A. H. Yazdavar, E. F. El-Saadany, and K. Ponnambalam, "On the loadability and voltage stability of islanded AC–DC hybrid microgrids during contingencies," *IEEE Syst. J.*, vol. 13, no. 4, pp. 4248–4259, Dec. 2019.
[17] J. Chen, F. Milano, and T. O'Donnell, "Assessment of grid-feeding converter voltage stability," *IEEE Trans. Power Syst.*, vol. 34, no. 5, pp. 3980–3982, Sep. 2019, doi: 10.1109/TPWRS.2019.2920516.
[18] Q. Ye, R. Mo, and H. Li, "Impedance modeling and DC bus voltage stability assessment of a solid-state-transformer-enabled hybrid AC–DC grid considering bidirectional power flow," *IEEE Trans. Ind. Electron.*, vol. 67, no. 8, pp. 6531–6540, Aug. 2020, doi: 10.1109/TIE.2019.2937039.
[19] D. L. H. Aik and G. Andersson, "Fundamental analysis of voltage and power stability of single-infeed voltage-source converter HVDC systems," *IEEE Trans. Power Del.*, vol. 34, no. 1, pp. 365–375, Feb. 2019, doi: 10.1109/TPWRD.2018.2874335.
[20] J. Chen, R. Zhu, T. O'Donnell, and M. Liserre, "Smart transformer and low frequency transformer comparison on power delivery characteristics in the power system," in *Proc. AEIT*, Bari, Italy, 2018, pp. 1–6.
[21] M. T. A. Khan, A. A. Milani, A. Chakrabortty, and I. Husain, "Dynamic modeling and feasibility analysis of a solid-state transformer-based power distribution system," *IEEE Trans. Ind. Appl.*, vol. 54, no. 1, pp. 551–562, Jan. 2018, doi: 10.1109/TIA.2017.2757450.
[22] Y. Tu, J. Chen, H. Liu, and T. O'Donnell, "Smart transformer modelling and hardware in-the-loop validation," in *Proc. IEEE 10th Int. Symp. Power Electron. Distrib. Gener. Syst. (PEDG)*, Xi'an, China, Jun. 2019, pp. 1019–1025.
[23] A. A. Milani, M. T. A. Khan, A. Chakrabortty, and I. Husain, "Equilibrium point analysis and power sharing methods for distribution systems driven by solid-state transformers," *IEEE Trans. Power Syst.*, vol. 33, no. 2, pp. 1473–1483, Mar. 2018, doi: 10.1109/TPWRS.2017.2720540.

JUNRU CHEN (Member, IEEE) received the M.E. and Ph.D. degrees in electrical energy engineering from University College Dublin, Dublin, Ireland, in 2016 and 2019, respectively. He was an Exchanging Student with Kiel University, Kiel, Germany, in 2018, and Tallinn University of Technology, Tallinn, Estonia. He was a Senior Researcher with University College Dublin and a Visiting Scholar with Aalborg University, Aalborg, Denmark, in 2020. Since 2020, he has been an Associate Professor with Xinjiang University, Ürümqi, China. His current research interests include power electronics control, modeling, stability, and application.

YI ZHANG (Student Member, IEEE) is currently pursuing the M.E. degree with the School of Electrical Engineering, Xinjiang University, Ürümqi, China. Her research interests include smart solid-state transformers and stability analysis.

MUYANG LIU (Member, IEEE) received the M.E. and Ph.D. degrees in electrical energy engineering from University College Dublin, Dublin, Ireland, in 2016 and 2019, respectively. From December 2019 to December 2020, she was a Senior Researcher with University College Dublin. She joined Xinjiang University, Ürümqi, China, in 2019, where she is currently an Associate Professor in electrical engineering. Her current research interests include power system modeling and stability analysis.

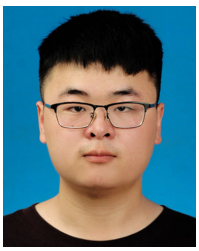

YUTIAN CHEN (Student Member, IEEE) received the master's degree in hydraulic and hydropower engineering from the Department of Electrical Engineering, Xinjiang University, Ürümqi, China, in 2023, where he is currently pursuing the Ph.D. degree with the College of Electrical Engineering. His research interests include renewable energy integration into the grid, power system frequency stability, and the operation control of virtual power plants.

RONGWU ZHU (Senior Member, IEEE) received the B.Eng. degree in electrical engineering from Nanjing Normal University, Nanjing, China, in 2007, and the Ph.D. degree in energy technology from the Department of Energy Technology, Aalborg University, Aalborg, Denmark, in 2015. From 2011 to 2012, he was a Guest Researcher with Aalborg University. From 2016 to 2021, he was a Senior Researcher with the Chair of Power Electronics, Christian-Albrechts-University of Kiel, Kiel, Germany. He is currently a Full Professor and the Director of Department of Electrical Engineering, Harbin Institute of Technology, Shenzhen, China. He has authored and coauthored around 130 technical articles (more than 1/3 of them in international peer-reviewed journals/magazine), and six patents. His research interests include renewables integration, control, operation, and the digitalization of power electronics, and renewables-dominated grid. He was an Editor of the *International Transactions on Electrical Energy System*, an Associate Editor of *Renewable Power Generation*, an Associate Editor of IEEE Open Journal of Power Electronics, and a Guest Associate Editor of IEEE Journal of Emerging and Selected Topics in Power Electronics, the Guest Editor-in-Chief of the *CSEE Journal of Power and Energy Systems*, and the Technical Committee Chair and a member for several international conferences. (Based on document published on January 2023).